Electronic Supplementary Material (ESI) for Catalysis Science & Technology.

Supporting Information for

The Catalytic Decomposition of Nitrous Oxide and the NO + CO Reaction over Ni/Cu Dilute and Single Atom Alloy Surfaces: First-principles Microkinetic Modelling

Konstantinos G. Papanikolaou and Michail Stamatakis*

Thomas Young Centre and Department of Chemical Engineering, University College London,

Roberts Building, Torrington Place, London WC1E 7JE, UK

1. Adsorption of N_2O on Rh(111), Cu(111), Ni/Cu(111) SAA and $Ni_2Cu(111)$

Figure S1 shows the six identified N_2O adsorption structures, and Table S1 summarises the computed adsorption energies and bond lengths.

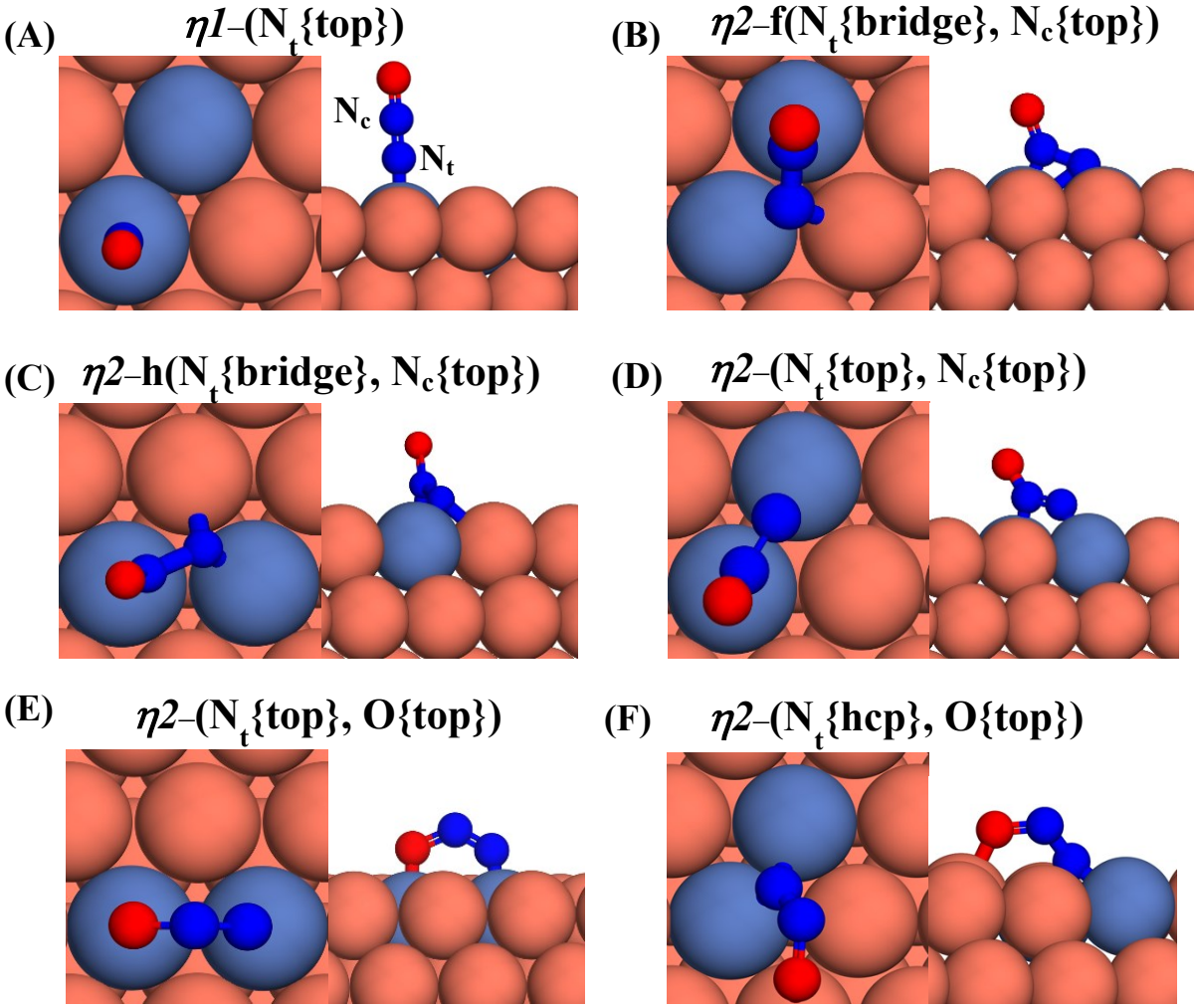

Figure S1. Top and side views of (A) η1–(N_t{top}); (B) η2–f(N_t{bridge},N_c{top}); (C) η2–h(N_t{bridge},N_c{top}); (D) η2–(N_t{top},N_c{top}); (E) η2–(N_t{top},O{top}) and (F) η2–(N_t{hcp},O{top}) adsorption structure. On the side view of (a) we highlight the terminal (N_t) and central(N_c) nitrogen atoms. Ni, Cu, N and O atoms are shown in purple, orange, blue and red, respectively. The adsorption geometries are shown over $Ni_2Cu(111)$, but they are representative for all surfaces

Table S1. Adsorption energies (in eV) and bond distances (in Å) for the different N_2O* adsorption geometries over the investigated surfaces. The adsorption energies and bond distances that correspond to the most stable adsorption structure(s) for each surface are shown in bold. A dash indicates either that the adsorption structure is not stable on the specific surface or that it is not a minimum on the potential energy surface (i.e. there was an imaginary frequency in the vibrational analysis). For comparison: $d_{N\text{-}N}$ = 1.14 Å and $d_{N\text{-}O}$ = 1.20 Å for gas N_2O.

Adsorption Structure	Property	Rh(111)	Cu(111)	Ni/Cu(111) SAA	Ni_2Cu(111)
η1*–(N_t{top})** (denoted as ***η1)	$E_{ads}(N_2O)$	-0.71	-0.21	**-0.70**	-0.68
	$d_{N\text{-}O}$	1.20	1.20	**1.20**	1.21
	$d_{N\text{-}N}$	1.15	1.15	**1.15**	1.15
η2–f(N_t{bridge},N_c{top}) (denoted as ***η2NbNt***)	$E_{ads}(N_2O)$	**-0.83**	+0.15	-0.43	**-0.74**
	$d_{N\text{-}O}$	**1.22**	1.23	1.23	**1.23**
	$d_{N\text{-}N}$	**1.35**	1.29	1.29	**1.31**
η2–h(N_t{bridge},N_c{top})	$E_{ads}(N_2O)$	**-0.83**	+0.15	-0.41	-0.73
	$d_{N\text{-}O}$	**1.22**	1.23	1.23	1.23
	$d_{N\text{-}N}$	**1.36**	1.29	1.28	1.30
***η2*–(N_t{top},N_c{top})**	$E_{ads}(N_2O)$	-0.68	+0.27	–	-0.62
	$d_{N\text{-}O}$	1.25	1.23	–	1.24
	$d_{N\text{-}N}$	1.26	1.22	–	1.25
η2–(N_t{top},O{top}) (denoted as ***η2NtOt***)	$E_{ads}(N_2O)$	-0.72	-0.20	-0.53	-0.68
	$d_{N\text{-}O}$	1.33	1.28	1.30	1.32
	$d_{N\text{-}N}$	1.20	1.19	1.20	1.20
η2–(N_t{hcp},O{top})	$E_{ads}(N_2O)$	–	**-0.25**	-0.44	**-0.73**
	$d_{N\text{-}O}$	–	**1.30**	1.31	**1.32**
	$d_{N\text{-}N}$	–	**1.27**	1.25	**1.27**

2. Electronic structure analyses of N_2O adsorption modes

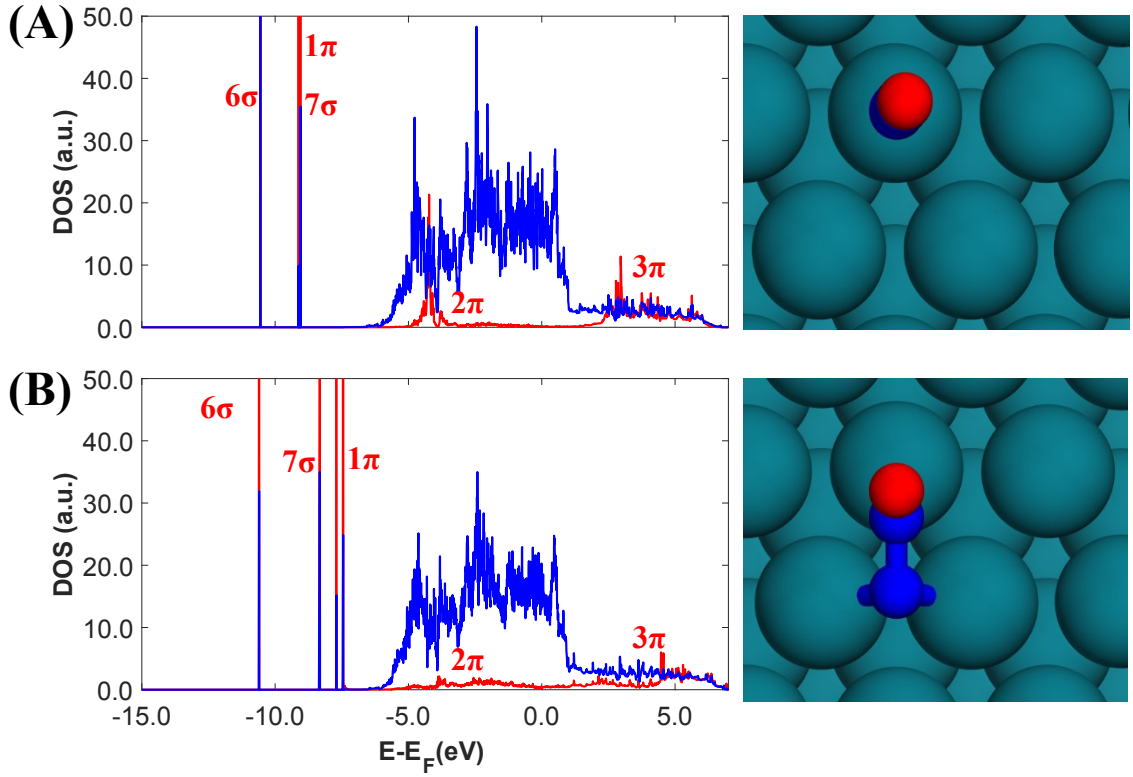

Figure S2. Projected density of states for (A) the *η1*-(N_t{top}); and (B) the *η2*-h(N_t{bridge}, N_c{top}) on Rh(111). The red line is the N_2O* contribution and the blue line is the metal contribution (only Rh surface atoms). The relaxed adsorption structures are shown on the right of each panel. Rh, O and N atoms are shown in dark green, red and blue.

3. Reaction path for N_2O formation and decomposition

Figure S3 shows the reaction path for the decomposition of N_2O to either NO* + N* or N_2* + O*. The energies presented are referenced to a non–interacting N_2O molecule in the gas–phase and a clean Rh(111) slab. For an accurate comparison of our results to the work of Paul et al.,[1] all the energies presented include the zero point energy (ZPE) correction, which can be introduced by calculating the energy of an adsorbed state as

$$E_{DFT,s} = E_{DFT}^{Slab+N_2O} - E_{DFT}^{Slab} - E_{DFT}^{N_2O_{(g)}} + \hbar\left(\sum_{i=1}^{9}\frac{\omega_i}{2} - \sum_{i=1}^{3}\frac{\omega_{N_2O,i}}{2}\right), \quad \text{(S1)}$$

where $E_{DFT,s}$ is the energy of a state s; $E_{DFT}^{Slab+N_2O}$, E_{DFT}^{Slab} and $E_{DFT}^{N_2O_{(g)}}$ are the DFT energies for a Rh(111) slab whereon N_2O is adsorbed, clean Rh(111) slab and a gas-phase N_2O molecule; $\hbar$ is the reduced Planck constant; $\omega_{N_2O,i}$ is the the angular frequency of the i^{th} mode of gas-phase N_2O and ω_i is the angular frequency of the i^{th} mode of N_2O in an adsorbed state.

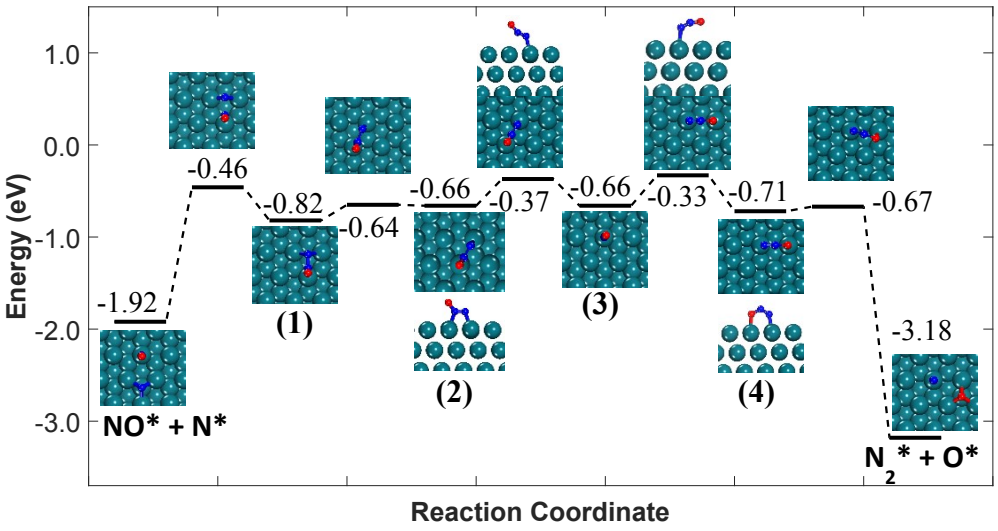

Figure S3. Reaction path for the decomposition of N_2O* either to NO* + N*or to N_2* + O*. The energy values are ZPE–corrected. The numbering of the adsorbed configurations of N_2O is as follows: (1) *η2*-f(N_t{bridge},N_c{top}), (2) *η2*-(N_t{top},N_c{top}), (3) *η1*-(N_t{top}) and (4) *η2*-(N_t{top},O{top}). Rh, O and N atoms are shown in dark green, red and blue, respectively.

4. NO* – NO* repulsive interactions

To demonstrate the NO* – NO* repulsive interactions, we plot the average adsorption energy of NO* over Rh(111) for different NO* surface coverages. As seen, at increasing surface coverage the NO* binding strength diminishes (i.e. less exothermic adsorption).

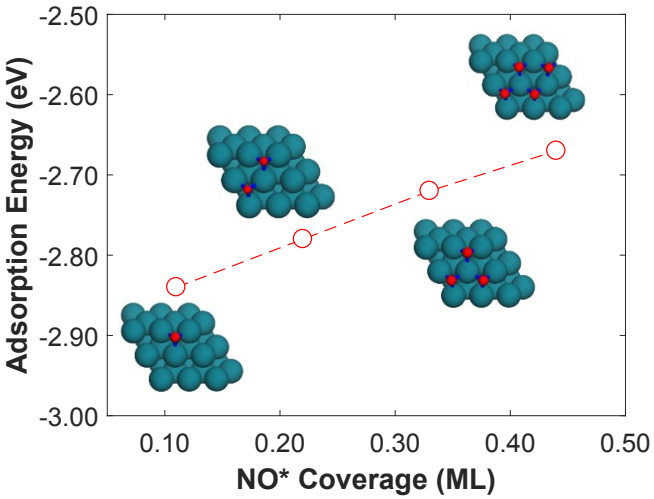

Figure S4. Average adsorption of NO* for various coverages. Rh, O and N atoms are shown in dark green, red and blue, respectively.

5. N_2O* formation *via* $(NO)_2$* on $Ni_3Cu(111)$

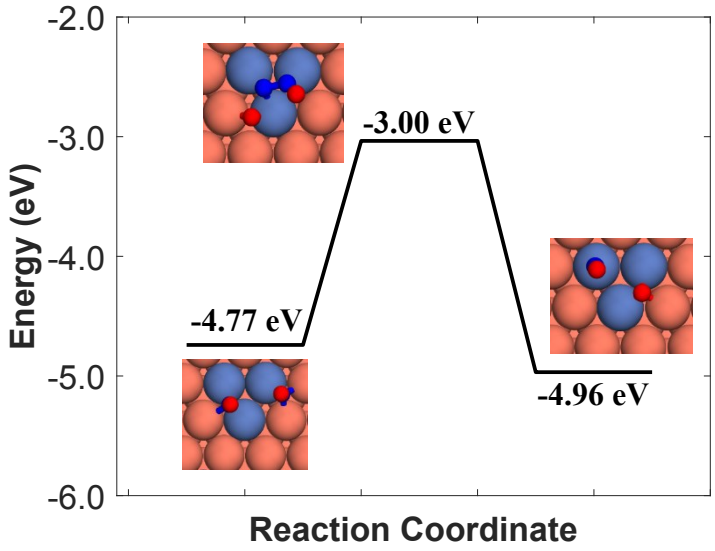

Figure S5. N_2O* formation via $(NO)_2$* on $Ni_3Cu(111)$.

6. Side views of the states within the N_2O* formation and decomposition reaction pathways

The following figures show the side view of the different states that are involved in the N_2O* formation/decomposition pathways (see Figure 2, Figure 3 and Figure 4 in the main text). The images are for the $Ni_2Cu(111)$ surface, but in the vast majority of cases they are representative for all the Cu–based surfaces.

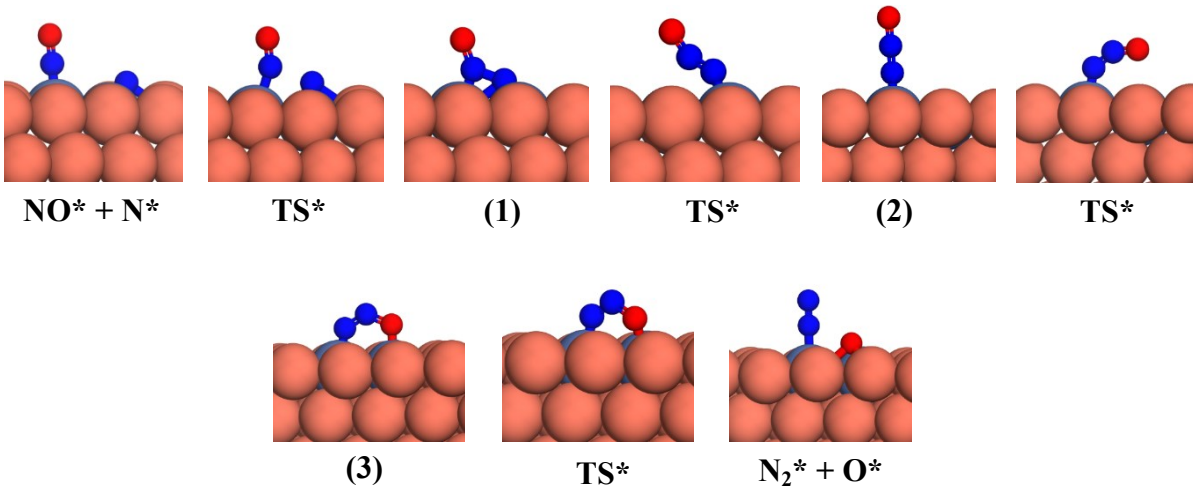

Figure S6. Side views of the states in Figure 2 (B) of the main text. Ni, Cu, O and N atoms are shown in purple, orange, red and blue, respectively.

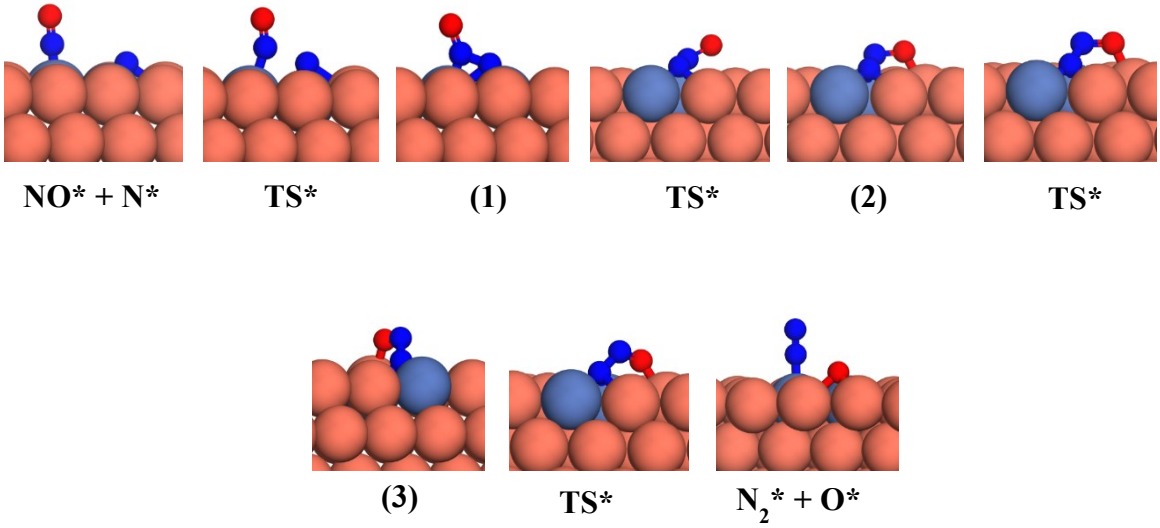

Figure S7. Side views of the states in Figure 3 (C) of the main text. Ni, Cu, O and N atoms are shown in purple, orange, red and blue, respectively.

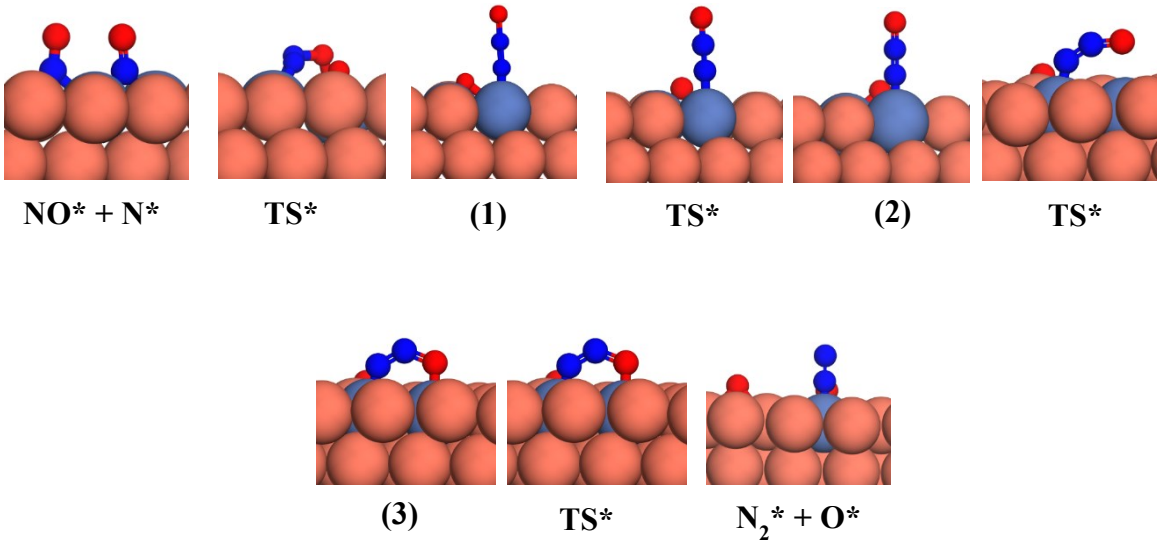

Figure S8. Side views of the states in Figure 4 (C) of the main text. Ni, Cu, O and N atoms are shown in purple, orange, red and blue, respectively.

7. O_2* association and NO_2* formation

Figure S9 shows the initial, transition and final states for the formation of O_2* from two O* adatoms. Also shown are the computed DFT energies for each structure.

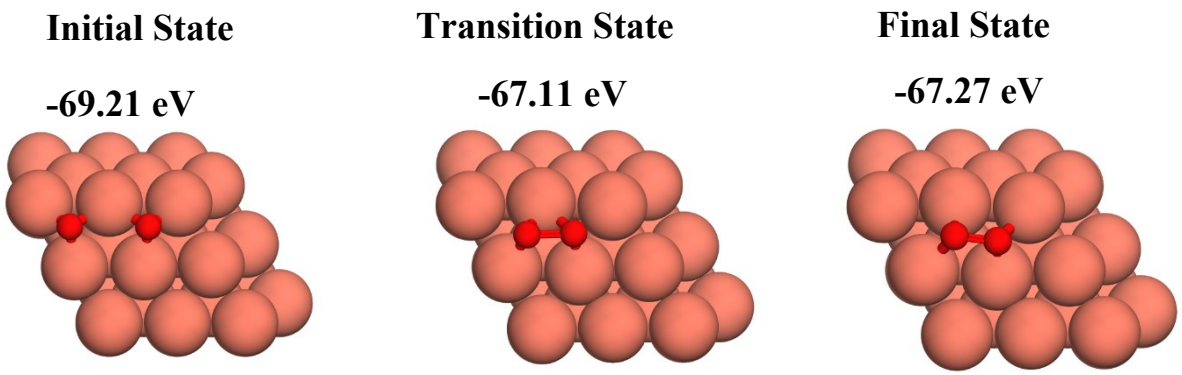

Figure S9. Top view of initial, transition and final states for the formation of O_2* on Cu(111). Cu and O atoms are shown in orange and red, respectively.

Regarding the NO_2* formation, we find that on Cu–based the forward barrier is always larger than 0.70 eV, while the reverse barrier (i.e. NO_2* dissociation) is always smaller than 0.30 eV. Our data indicates that the formation of NO_2* is neither kinetically nor thermodynamically favoured. The most stable final state for all the three surfaces is the so-called μ-N,O-nitrito adsorption mode, whose stability is experimentally confirmed on other coinage metal surfaces.[2] We also compute the adsorption energies of NO_2* in the μ-N,O-nitrito structure on the Cu-based surfaces (Table S2). The obtained values imply that even if NO_2* is formed on the surface its dissociation will be dramatically more favourable than its desorption, thereby corroborating our reaction mechanism, which does not take into account the formation of NO_2*.

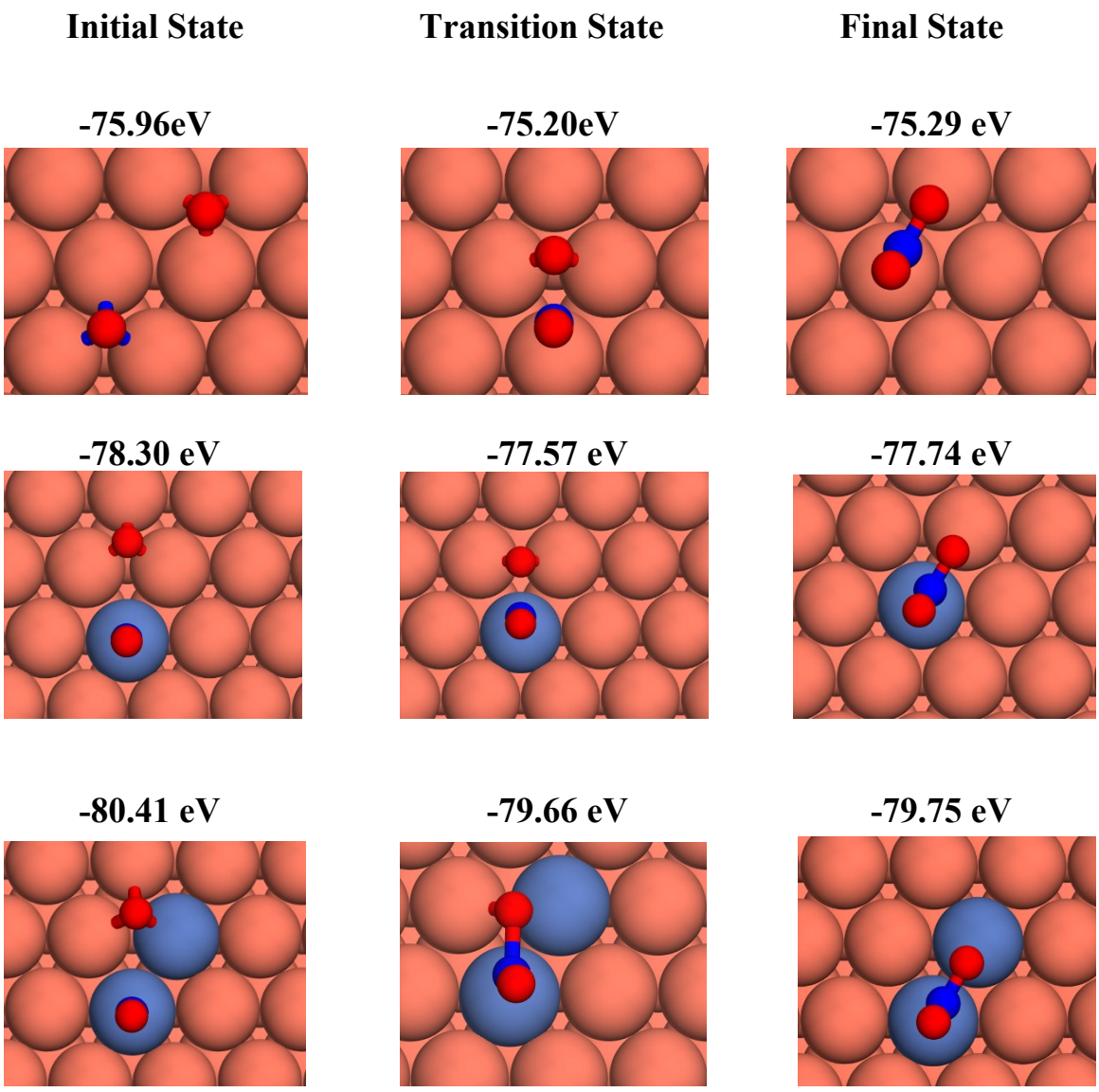

Figure S10. Top view of initial, transition and final states for the formation of NO_2* on Cu(111), Ni/Cu(111) SAA and Ni_2Cu(111) surfaces. Ni, Cu, O and N atoms are shown in purple, orange, red and blue, respectively.

Table S2. Adsorption energies for NO_2* in μ-N,O-nitrito adsorption structure on Cu-based surfaces. Note that the gas-phase calculation for $NO_{2(g)}$ was spin-polarised.

Surface	**$E_{ads}(NO_2)$**
Cu(111)	-1.70 eV
Ni/Cu(111) SAA	-2.10 eV
$Ni_2Cu(111)$	-2.30 eV

8. Activity plot for Cu(111) at “low temperatures”

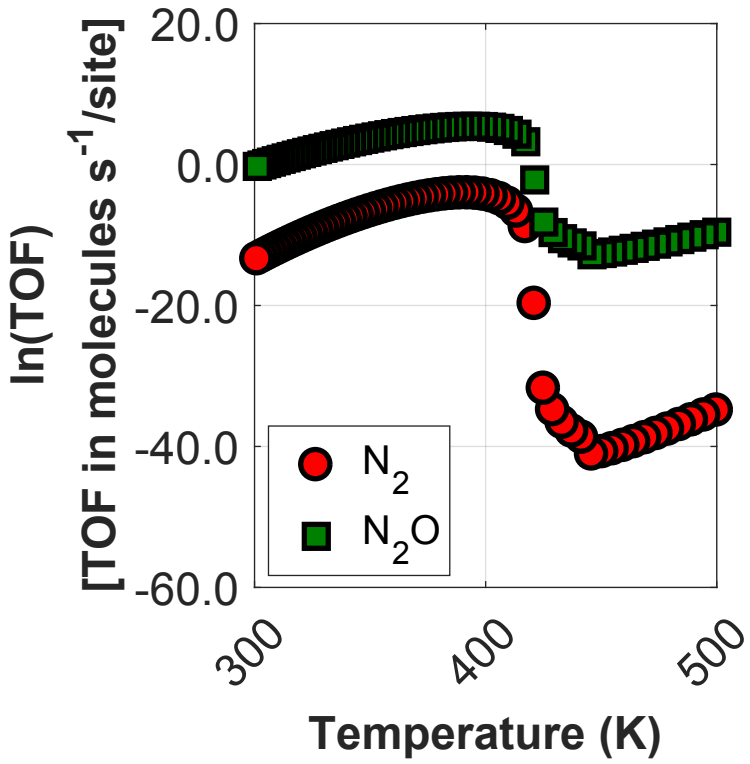

Figure S11. Activity of Cu(111) within the temperature range of 300 K – 500 K (Low-temperature range).

9. Explanation for the selectivity peak on Ni/Cu bimetallic alloys

Figure S12 (A) and (B) shows that the selectivity peak of $Ni_2Cu(111)$ is unaffected by changes to the activation barrier to the formation of N_2* (R16 in Table 2 in the main text) and the dimerization reaction (R15 in Table 2 in the main text) on Ni*. On the contrary, the peak (which appears between 950 K and 1400 K) disappears upon increasing the activation barrier for the formation of N_2O* (R9 in Table 2 in the main text) and NO* dissociation (R8 in Table 2 in the main text) reactions on Ni*. Therefore, the selectivity spike for Ni/Cu SAA and Ni_2Cu in Figure 7 (A) is associated only with the latter two reactions.

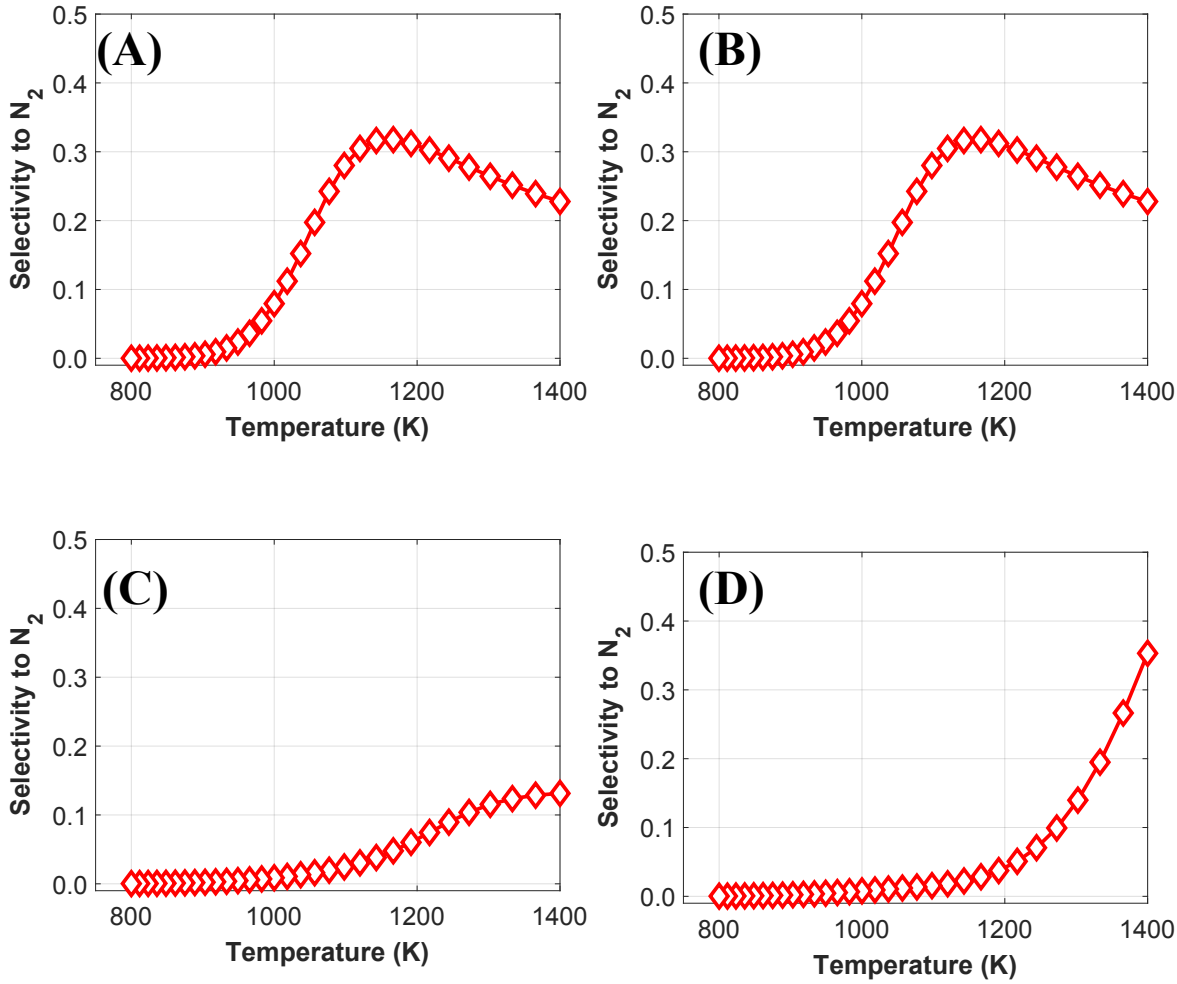

Figure S12. Predicted selectivity to N_2 after setting a large activation barrier (i.e. 2.5 eV) for (A) the formation of N_2* on Ni*; (B) the dimerization reaction on Ni*; (C) the direct dissociation of NO* on Ni*; and (C) the formation of N_2O* on Ni*

10. Sites involved in surface reactions over Ni/Cu bimetallic alloys

Several elementary events in our microkinetic model involve two sites, which may be of different type on the Ni/Cu bimetallic alloys. On the latter surfaces, the two–site reactions (see Table 2) can happen either on Cu sites, where the reactants and products are on Cu*, or on pair of sites that include both Ni* and Cu*. Table S3 tabulates the two-site events of the NO + CO reaction along with the site types whereon the reactant and product adspecies are adsorbed in our model.

Table S3. Two–site events and sites where reactant and product species are adsorbed. The adsorption sites (i.e. either Ni*or Cu*) are shown in bold. Also in bold are the reaction numbers, which correspond to the numbers shown in Table 2 in the main text. Empty sites are denoted as Ni* or Cu*. For occupied sites, the adsorbate is specified followed by the site type in parenthesis.

Reaction	Reactant 1	Reactant 2	Product 1	Product 2
NO* + * ↔ N* + O* **(R8)**	NO* (**Ni***)	**Cu***	N* (**Ni***)	O* (**Cu***)
NO* + N*↔ N_2O* *η2NbNt* + * **(R9)**	NO* (**Ni***)	N* (**Cu***)	N_2O* *η2NbNt* (**Ni***)	**Cu***
N_2O* *η2NtOt* + * ↔ N_2* + O* **(R12)**	N_2O* *η2NtOt* (**Ni***)	**Cu***	N_2* (**Ni***)	O* (**Cu***)
N_2O* *η2NbNt* + * ↔ N_2* + O* **(R13)**	N_2O* *η2NbNt* (**Ni***)	**Cu***	N_2* (**Ni***)	O* (**Cu***)
CO* + O* ↔ CO_2* + * **(R14)**	CO* (**Ni***)	O* (**Cu***)	CO_2* (**Ni***)	**Cu***
NO* + NO* ↔ N_2O* *η1* + O* **(R15)**	NO* (**Ni***)	NO* (**Cu***)	N_2O* *η1* (**Ni***)	O* (**Cu***)
N* + N* ↔ N_2* + * **(R16)**	N* (**Ni***)	N* (**Cu***)	N_2* (**Ni***)	**Cu***

11. Computed adsorption energy for N_2O* using different vdW functionals

Table S4 tabulates the $E_{ads}(N_2O)$ for the three different adsorption geometries that are considered in the microkinetic model, computed using different exchange-correlation (XC) functionals, in particular: optPBE–vdW, optB86b–vdW, BEEF–vdW, and the Tkatchenko–Scheffler method (DFT–TS). Our results suggest that binding strengths that are predicted by different XC vdW functionals are considerably different, and this a known and non–trivial challenge in DFT calculations where nonlocal effects are accounted for.[3] Therefore, the result of microkinetic simulations will strongly depend on the performance of the selected XC functional. For example, for the NO + CO reaction, one should expect that the selectivity peak of Figure 7 (A) will be higher than 0.65 if optPBE–vdW is used. By contrast, values of 0.25 or less can be expected if the DFT–TS or BEEF-vdW are employed.

Table S4. Cu lattice constants and N_2O* adsorption energies (in eV) using different vdW treatments. Adsorption energies are presented only for the three N_2O* geometries that are taken into account in the microkinetic model of the NO + CO reaction and are computed on the $Ni_2Cu(111)$ surface. Lattice constants are reported in Å and the experimentally determined value is 3.596 Å.

XC Functional	$E_{ads}(\eta 1)$	$E_{ads}(\eta 2NbNt)$	$E_{ads}(\eta 2NtOt)$	Lattice Constant (Cu)
optPBE–vdW	-0.93	-0.91	-0.95	3.648
optB86b–vdW*	-0.67	-0.74	-0.68	3.608
DFT–TS	-0.40	-0.56	-0.48	3.635
BEEF–vdW	-0.33 ± 0.14	-0.17 ± 0.23	-0.24 ± 0.31	3.661

***** used functional in this work

References

1 J.-F. Paul, J. Pérez-Ramírez, F. Ample and J. M. Ricart, *J. Phys. Chem. B*, 2004, **108**, 17921–17927.

2 M. E. Bartram and B. E. Koel, *Surf. Sci.*, 1989, **213**, 137–156.

3 S. Gautier, S. N. Steinmann, C. Michel, P. Fleurat-Lessard and P. Sautet, *Phys. Chem. Chem. Phys.*, 2015, **17**, 28921–28930.